LUND UNIVERSITY

In-situ characterization of metal nanoparticles and their organic coatings using laser-vaporization aerosol mass spectrometry

Nilsson, Patrik; Eriksson, Axel; Ludvigsson, Linus; Messing, Maria; Nordin, Erik; Gudmundsson, Anders; Meuller, Bengt; Deppert, Knut; Fortner, Edward; Onasch, Timothy; Pagels, Joakim

In-situ characterization of metal nanoparticles and their organic coatings using laser-vaporization aerosol mass spectrometry

Patrik T. Nilsson[1] (✉), Axel C. Eriksson[1,2], Linus Ludvigsson[3], Maria E. Messing[3,4], Erik Z. Nordin[1], Anders Gudmundsson[1], Bengt O. Meuller[3], Knut Deppert[3], Edward C. Fortner[5], Timothy B. Onasch[5], and Joakim H. Pagels[1]

[1] *Ergonomics and Aerosol Technology, Lund University, P.O. Box 118, Lund SE-22100, Sweden*
[2] *Nuclear Physics, Lund University, P.O. Box 118, Lund SE-22100, Sweden*
[3] *Solid State Physics, Lund University, P.O. Box 118, Lund SE-22100, Sweden*
[4] *Synchrotron Radiation Research, Lund University, P.O. Box 118, Lund SE-22100, Sweden*
[5] *Aerodyne Research Inc., Billerica, MA 01821-3976, USA*

ABSTRACT

The development of methods to produce nanoparticles with unique properties via the aerosol route is progressing rapidly. Typical characterization techniques extract particles from the synthesis process for subsequent offline analysis, which may alter the particle characteristics. In this work, we use laser-vaporization aerosol mass spectrometry (LV-AMS) with 70-eV electron ionization for real-time, *in-situ* nanoparticle characterization. The particle characteristics are examined for various aerosol synthesis methods, degrees of sintering, and for controlled condensation of organic material to simulate surface coating/functionalization. The LV-AMS is used to characterize several types of metal nanoparticles (Ag, Au, Pd, PdAg, Fe, Ni, and Cu). The degree of oxidation of the Fe and Ni nanoparticles is found to increase with increased sintering temperature, while the surface organic-impurity content of the metal particles decreases with increased sintering temperature. For aggregate metal particles, the organic-impurity content is found to be similar to that of a monolayer. By comparing different equivalent-diameter measurements, we demonstrate that the LV-AMS can be used in tandem with a differential mobility analyzer to determine the compactness of synthesized metal particles, both during sintering and during material addition for surface functionalization. Further, materials supplied to the particle production line downstream of the particle generators are found to reach the generators as contaminants. The capacity for such *in-situ* observations is important, as it facilitates rapid response to undesired behavior within the particle production process. This study demonstrates the utility of real-time, *in-situ* aerosol mass spectrometric measurements to characterize metal nanoparticles obtained directly from the synthesis process line, including their chemical composition, shape, and contamination, providing the potential for effective optimization of process operating parameters.

Address correspondence to patrik.nilsson@design.lth.se

1　Introduction

The field of nanotechnology developed significantly during the past decade, and the current potential for the creation of materials with novel characteristics has facilitated the realization of almost unlimited numbers of nanomaterial and nanoparticle applications [1, 2]. As a result of the growing demand for such products, there is currently a need for new production methods with increased throughput and high reliability. In particular, aerosol production methods are attractive, as they can be performed in a continuous manner and particles with high purity and tailored morphologies can be synthesized [3].

Aerosol production, or aerosol synthesis, methods are based on the formation of particles from a gas, liquid, or solid material. The optimal synthesis method for a given product depends on the desired characteristics of the resultant particles and the required quantity. After synthesis, metal nanoparticles are typically modified through heat treatment (e.g., sintering to more compact shapes), surface functionalization via chemical reactions, and/or condensation of additional material. The synthesized particles can be subjected to various degrees of post-treatment in order to alter their characteristics; thus, methods to study the effects and performance of such particle treatments are necessary [3].

At present, aerosol synthesis methods are hampered by a lack of development of instruments that can be used to analyze and characterize the synthesized particles *in-situ* and in real-time [4]. Current state-of-the-art particle analysis involves offline techniques such as electron microscopy, X-ray diffraction [5], and X-ray photoelectron spectroscopy [6]. A disadvantage of these techniques is that, under the majority of circumstances, the aerosol particles must be extracted from the production line and collected on different types of substrates prior to analysis. The particle characteristics (e.g., their morphology, surface properties, oxidation, and impurity levels) may be altered during the collection, storage, or analysis stages. Such alterations are important, as impurities, which can be present as complete or partial coatings on the particles, can have a significant impact on the realization of the ultimate intended particle performance. To avoid this problem, one approach is to analyze the particles directly in the aerosol phase and on the production line.

Thus, a real-time instrument that simultaneously quantifies and determines the chemical composition, size, and morphology of particles on the production line can be considered to be the optimal aerosol analytical instrument. Aerosol mass spectrometry is comprised of a series of techniques, through which gas-borne particles are sampled directly from the aerosol phase into a vacuum chamber, vaporized, ionized, and then detected using mass spectrometry. Some of these techniques rely upon combined laser vaporization and desorption. However, such approaches are limited in terms of quantification [7]. Electron-ionization aerosol mass spectrometry (EI-AMS, or simply AMS) was originally developed for the study of atmospheric aerosols [8, 9], however, its applications have recently been expanded [10–12]. With AMS, one can determine the chemical compositions of sampled particles as well as the particle size distributions and total particle mass concentrations of non-refractory species (species that flash vaporize at $600\ ^\circ\text{C}$) [13], including certain volatile metal species [14]. Recently, further refinements to AMS have facilitated the detection of refractory species such as carbon black and metal-containing particles [15, 16]. This refined instrument is commonly referred to as the soot-particle aerosol mass spectrometer (SP-AMS) and uses intracavity infrared (IR) laser vaporization followed by 70-eV electron ionization.

The sensitivity of the SP-AMS to metals internally mixed (existing within the same particles) at trace amounts within carbon-black particles has been reported [17]. In such studies, the carbon-black core acts as the vaporizer (heated to $4{,}000\ \text{K}$ before vaporization). These approaches are important for atmospheric applications, but they have only limited application to engineered nanoparticles.

In this work, we aim to explore the potential application of the SP-AMS technique as a tool for the investigation of important characteristics of synthesized metal nanoparticles. Therefore, we have chosen to refer to this instrument as the laser-vaporization aerosol mass spectrometer (LV-AMS), which reflects its broader applications. We show that the LV-AMS can be used

to determine important chemical and physical characteristics of metal particles in real-time, such as their alloy composition, degree of oxidation, impurity type and content, size, and morphology. We show that the LV-AMS can be used to characterize and compare different metal-nanoparticle synthesis techniques and demonstrate how post-production sintering and condensation of functionalization material may affect metal nanoparticles. *In-situ* analysis apparatus like the LV-AMS are important for the development and understanding of new synthesis methods, for product quality optimization, and for production process control.

2 Experimental

2.1 Particle-generation setups

Metal particles were synthesized using two different types of apparatus: (1) spark-discharge generators (SDG) and (2) a high-temperature furnace (HTF). The general experimental setup including the particle-synthesis, size-selection, sintering, organic-surface-coating, and particle-characterization equipment is shown in Fig. 1. The metal particles generated using the SDG setups were Ag, Au, Cu, Fe, Ni, Pd, and PdAg nanoalloys. The HTF was used to generate Au and Ag nanoparticles.

A SDG consists of a particle-generation chamber that houses two metal electrodes separated by a few millimeters. When a high voltage is applied to the electrodes, a spark is formed. The high temperature generated by the spark instantly evaporates metal from the electrodes and metal particles are subsequently formed through nucleation, condensation, and coagulation of these vapors. The formed particles are aggregates with a typical primary particle size of 5–7 nm and average aggregate geometric mean diameters (GMD) of 20–40 nm. The metal compositions of the two electrodes and their separation distance can be adjusted in order to vary the chemical composition, size, and morphology of the generated metal nanoparticles. During this study, two different SDG instruments were used: (i) SDG_P (GFG 1000, Palas, Karlsruhe, Germany) and (ii) SDG_C (system constructed in-house) [18].

The HTF apparatus consists of a tube furnace with a graphite or ceramic tube. The desired particle base materials are placed in a crucible inside the tube furnace and heated to the required temperature. The particles formed by the HTF are aggregates with similar primary particle sizes to those formed with the SDG. The average GMD of the HTF-generated aggregates is 50–100 nm. The chemical composition, size, and morphology of the generated metal nanoparticles are dependent on the evaporated material type and content, the furnace temperature, and the carrier-gas flow rate.
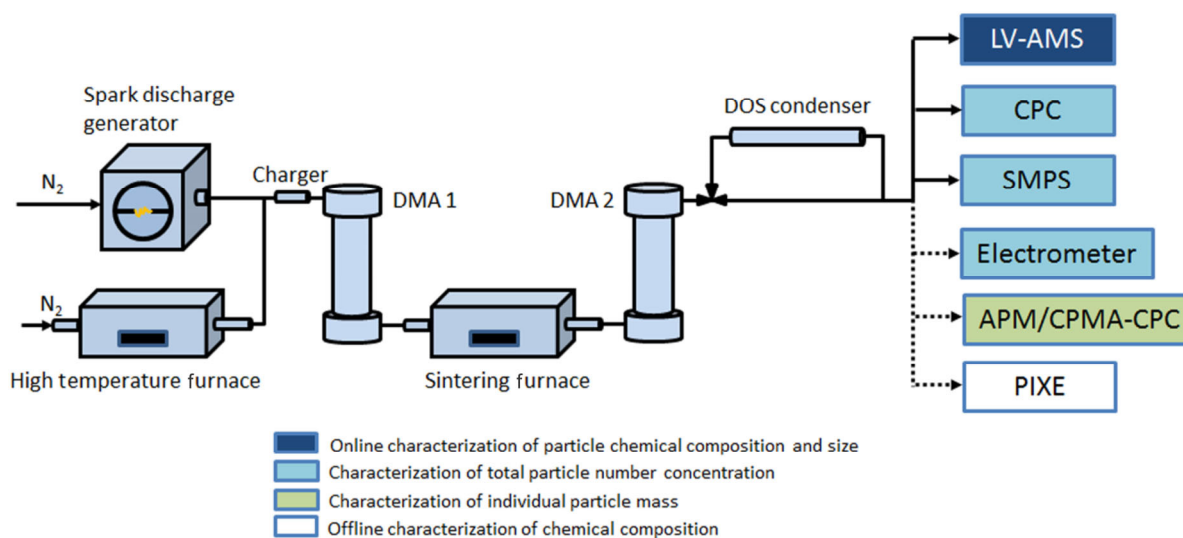

Figure 1 Schematic of particle-generation and transformation setup, and instruments used for particle characterization. The instruments connected by dashed arrows were used for selected particle types.

In this study, after the metal-particle generation using either SDG or HTF, the particles were size-selected using a differential mobility analyzer (DMA) and passed through a sintering furnace. The furnace was used to heat the aggregate particles to a sintering temperature, i.e., the temperature at which the aggregates collapsed to near-spherical shapes. DMAs were used both upstream and downstream of the sintering furnace to select particles with specific mobility particle sizes and to measure the changes in this characteristic during sintering.

Typically, an aerotaxy system that is used for nanowire growth with the produced metal particles as seeds is connected downstream from the metal-particle generation setup, as depicted in Fig. 1. However, this aerotaxy system, which is described in detail elsewhere [19], was not connected to the generator setup during the measurements presented in this paper. The influence of the aerotaxy system on the metal-generator setup was investigated by determining whether material supplied to the aerotaxy system could reach and contaminate the metal particle generators. This examination was performed after the aerotaxy system had been disengaged from the metal-particle generators, and maintenance and cleaning of the HTF was deliberately neglected. The nanowires produced in the aerotaxy system consisted of GaAs and were created by supplying trimethyl-gallium ($Ga(CH_3)_3$) and arsine (AsH_3) to the system.

For a small group of experiments, a condenser tube (13 mm-inside diameter (ID) Pyrex glass tube) was used to condense organic surface coatings on the metal nanoparticles after the sintering process, in order to study the effects on the particle chemical composition, size, and shape. The condenser tube was temperature-controlled up to 150 ℃ using two temperature zones, which were controlled using heating tape wrapped on the exterior of the glass tube. A non-refractory liquid organic model substance, dioctyl sebacete (DOS), was placed in a small Al container inside the condenser tube. The dual temperature zones enabled condensation control and the elimination of self-nucleated DOS particles. Three different types of Ag nanoparticles were used for the DOS condensation: aggregates, semi-sintered, and sintered particles, all with a single m_p of ~4 fg. The semi-sintered Ag particles were partly sintered at a temperature of 200 ℃ and the sintered

Ag particles were heated to a temperature of 900 ℃.

2.2   Instrumentation

In-situ characterization of the airborne nanoparticles was performed using a LV-AMS (Aerodyne Inc., Billerica MA, USA). This instrument is identical to the high-resolution time-of-flight AMS (HR-ToF-AMS), with the addition of an intracavity Nd:YAG laser (wavelength, $\lambda = 1{,}064$ nm) as a vaporization technique [15]. In atmospheric applications, this system is referred to as a SP-AMS. In AMS instruments, aerosol particles are focused into a tight particle beam in vacuum using an aerodynamic lens [8, 9]. Then, in conventional AMS, the focused particles are accelerated across a vacuum chamber to impact upon a heated W vaporizer that is typically set to 600 ℃. Upon the subsequent flash vaporization, the molecules are ionized through electron ionization (70 eV) and the resultant ions are extracted into a ToF-MS. Electron ionization at 70 eV is standard in an AMS. At this energy level, the electron-ionization cross sections, including those for carbon and organic molecules, are close to maximum. The ionization efficiencies (IE) for metal components are also maximized close to 70 eV [20]. A disadvantage of electron ionization is that the organic molecules are fragmented and it is difficult to identify the parent molecules in cases where the sampled aerosol consists of multiple unknown organic species. As no molecule separation can be performed prior to ionization, the chemical identification of organic molecules using AMS typically means that different molecular classes are identified and quantified, rather than the parent organic molecules. Studies have shown that AMS yields mass spectra that are similar to those provided in databases, such as the National Institute of Standards and Technology (NIST) database, for molecules that are resistant to thermal decomposition and fragmentation [21]. However, other molecule types, e.g., aliphatic organic molecules, may fragment as a result of the thermal vaporization preceding the ionization. For these types of molecules, the AMS mass spectra exhibit the same ion fragments as those found in the corresponding NIST mass spectra, but at different relative intensities [22]. Soft ionization techniques that use less energy than electron ionization and that may lead to less or no molecular fragmentation are currently being investigated for incorporation

with AMS. However, such techniques yield reduced ionization cross sections and are less versatile compared to electron ionization [9].

Non-refractory species, which evaporate below 600 °C, can be detected using the W vaporizer. The laser vaporizer in the LV-AMS is positioned in the vaporization zone, perpendicular to the particle beam. The laser vaporizer allows refractory and non-refractory species to be vaporized and detected when they are internally mixed with material that absorbs laser irradiation at 1,064 nm sufficiently, such as soot, metal, and selected metal-oxide particles. As the vaporization and ionization are separate, the number of formed ions is directly proportional to the vaporized-particle mass; this facilitates quantitative measurements of the particle mass concentration.

In this study, the LV-AMS was operated in two modes: the size-resolved particle ToF (PToF) mode and the size-integrated MS mode. In the size-resolved mode, the particle beam is modulated by a continuously rotating (140 Hz) mechanical chopper. The chopper has a small slit (2%) that allows the particle beam to pass once per chopper cycle. By timing the mechanical chopper cycle and ion detection in the MS, the vacuum aerodynamic diameter (d_{va}) and particle mass size distributions of the sampled particles can be determined. This is possible because the particle ToF (~3 ms) is significantly longer than that of the ion (~50 μs) in the MS [23].

When the chopper is alternated between open and closed positions (i.e., the particle beam is repeatedly blocked), an average background-corrected difference mass spectrum can be obtained for the sampled particles (in the MS mode). Unlike the PToF mode, the MS mode provides no size-resolved data, but exhibits higher sensitivity. In this study, data analysis was performed using the Sequential Igor Data Retrieval (SQUIRREL, version 1.56D Aerodyne Inc., Billerica MA, USA) and Peak Integration by Key Analysis (PIKA, version 1.15D Aerodyne Inc., Billerica MA, USA) software. The LV-AMS detection limits (3σ) for 1 min averaging were determined based on particle-filtered measurements of the sample aerosol.

The LV-AMS technique yields quantitative measurements after the mass-specific ionization efficiencies, mIE (in ions per pg), of the different metals and metal oxides are determined. These values depend on the

relative ionization efficiency of the metal relative to the calibration aerosol (RIE_s). The calibration aerosol may be nitrate [15] or regal black, a commercial carbon black [17]. The RIE_s is determined from the absorption cross sections for 70-eV metal ionization and the calibrate particles. In addition, the collection efficiency (CE) of each vaporizer configuration must be known. The overall CE of a vaporizer configuration is a function of the particle transmission through the sampling lens (E_L) and vaporizer-specific factors, such that

$$CE = E_L \times E_B \times E_S \times E_V \qquad (1)$$

where E_B indicates the influence of incomplete vaporization due to particle bounce from the vaporizer surface (W vaporizer), E_S is the effect of overlap mismatches between the sampled particle beam and the laser beam in the vaporization and detection chamber (laser vaporizer), and E_V represents the influence of incomplete vaporization due to limitations in the absorption cross section of the material at 1,064 nm (in this case). E_L is affected by losses in the sampling inlet at vacuum aerodynamic sizes above approximately 400 nm, which is of increased importance for increased particle sintering. The standard aerodynamic lens used in the LV-AMS permits penetration by particles smaller than 1,000 nm. The possibility to sample particles of larger aerodynamic diameters exists if a lens that allows penetration of particles up to 3,000–4,000 nm is employed [24]. For the heated W vaporizer, the CE is governed by E_B [25]. The E_B is expected to trend downward below unity for more compact metal nanoparticles (i.e., particles with a lower surface area for constant inertia), while non-refractory liquid coatings commonly decrease bounce.

For the laser vaporizer, the CE may be lower than unity as a result of E_S [26]. E_S tends to increase toward unity for increasingly spherical metal nanoparticles (i.e., there is less particle beam divergence because of the symmetric particle shapes), which occurs with increased sintering temperatures. When both vaporizers are in use, we expect to maximize the vaporizer-specific CE factors (i.e., E_B and E_S should be close to unity), especially as they trend in opposite directions with sintering. For metal and metal-oxide particles, E_V may also become a limiting factor.

This work represents one of the first direct applications of the LV-AMS technique for characterization of the sizes, mass concentrations, and chemical compositions of metal nanoparticles. We focus on demonstrating the potential benefits of this technique for *in-situ* characterization of metal nanoparticles; therefore, we assume that the CE is unity. Note that a CE of unity is expected to be a reasonable approximation for organic surface coatings, as both vaporizers contribute to this signal. However, this assumption most likely leads to underestimation of the metal concentrations, as the metals are vaporized by the laser vaporizer only. Therefore, the metal signals are reported in Hz only in this study; further quantification will be a topic of future research.

An aerosol particle mass analyzer (APM; Model 3600, Kanomax Inc., Japan) combined with a DMA was used to determine the mass per particle (m_p) and effective densities (ρ_{eff}) of the particles [27, 28]. In a small number of experiments, a centrifugal particle mass analyzer (CPMA) [29] replaced the APM so as to quantify the amount of DOS coatings present on the Ag particles. The APM or CPMA was placed downstream of a DMA that facilitated determination of the m_p for one mobility particle size at a time. Note that, once the m_p and mobility diameter (d_m) are known, the effective density $\rho_{eff(I)}$ can be calculated from

$$\rho_{eff(I)} = \frac{m_p}{\frac{\pi}{6} d_m^3} \qquad (2)$$

Here, the same nomenclature as that of DeCarlo et al. (2004) is used. Further, a second, closely related effective density $\rho_{eff(III)}$ can be determined from serial determination of d_m and d_{va} from the LV-AMS, such that

$$\rho_{eff(III)} = \frac{d_{va}}{d_m} \rho_0 \qquad (3)$$

where ρ_0 is the unit density. The various ρ_{eff}, which are determined using different methods, may differ in relation to each other, depending on the particle sizes and dynamic shape factors. The ρ_{eff} determined from mass-mobility relationships ($\rho_{eff(I)}$) and the vacuum aerodynamic size mobility ($\rho_{eff(III)}$) are highly correlated (i.e., they exhibit similar trends in response to particle

size and shape variations), and their values typically differ by less than 30% [30]. However, little experimental information is available on these differences.

The total particle number concentrations were determined using an electrometer constructed in-house and a condensation particle counter (CPC). Two CPCs were used alternately: a CPC 3010 (TSI Inc.) and a CPC 3022 (TSI Inc.) at flow rates of 1 and 0.3 lpm, respectively. The mobility particle size distributions were determined using a scanning mobility particle sizer (SMPS; DMA 3071 and CPC 3010, TSI Inc.).

Filter samples were collected for offline analysis of the metals via particle-induced X-ray emissions analysis (PIXE). The PIXE samples were collected on 37-mm polycarbonate filters (0.4-μm pore size, Nuclepore) contained in three-piece plastic filter cassettes. The flow rate through the filters was 1 lpm.

The organic mass fraction (m_{fOA}) on (or in) the engineered nanoparticles was determined by quantifying the mass concentration of the organic aerosol (C_{OA}) from the LV-AMS (as described in Onasch et al. (2012)), the total particle mass concentration based on the number concentration from the CPC (N) and the total m_p (metal + impurity) determined from either the APM/CPMA or the d_m and d_{va}. The m_{fOA} was calculated from

$$m_{fOA} = C_{OA} \cdot \frac{1}{N \cdot m_p} = \frac{I_{OA}}{RIE_{OA} \cdot CE \cdot mIE_{NO_3} \cdot Q} \cdot \frac{1}{N \cdot m_p} \qquad (4)$$

where I_{OA} is the sum of the signals for all organic ion fragments in Hz, RIE_{OA} is the ionization efficiency of organic aerosol relative to nitrate (here assumed to be 1.4), mIE_{NO_3} is the measured ionization efficiency of NO_3 (700 ions·pg^{-1}), and Q is the volumetric flow rate (1.47 cm^3·s^{-1}) of the LV-AMS. We conducted these measurements for both LV-AMS vaporizer configurations (dual vaporizers and the heated W vaporizer in isolation).

3   Results and discussion

3.1   Chemical analysis using high-resolution aerosol mass spectrometry

With the increased use of high resolution mass

spectrometry (HR-MS), the concept of mass defects has been increasingly exploited in MS data analysis [31]. A mass defect is defined as a deviation of a compound's exact mass from its nominal mass. This concept is used in HR-MS to differentiate between various detected ions with the same nominal mass-to-charge (m/z) ratio. In Fig. 2(a), the ^{107}Ag isotope can be separated from the main organic ion ($C_8H_{11}^+$), which is found at the same nominal m/z in this example. This facilitates the characterization of any non-refractory particulate matter (i.e., impurities) that may exist on metal particles. Impurities, such as organic ions, located at the same nominal m/z can also often be separated from each other, as their mass defects depend on the atomic compositions of the ions. For example, the addition of H (1.008 u) or O (15.995 u) atoms to an ion changes the mass defect in a positive or negative direction, respectively. As shown in Fig. 2(b), metals have a large
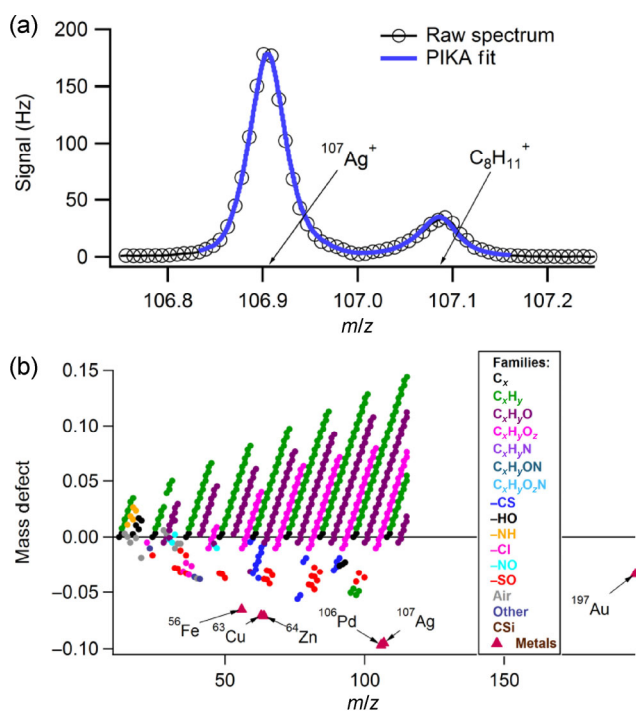
negative mass defect; thus, they are typically easy to identify in HR mass spectra. Therefore, chemical information on both metal nanoparticles and any potential impurities can be obtained using HR-MS.

3.2 Aerosol mass spectra of metal nanoparticles

Individual mass spectra achieved following sampling of synthesized metal nanoparticles from four different materials are shown in Fig. 3. Each mass spectrum contains indicators of ions corresponding to the different metal and metal-oxide isotopes (red) and organic impurities (green). To further improve the accuracy of the metal-ion identification, the isotopic abundances of the metal isotopes can be compared to reported values. These comparisons can also be used to evaluate the data analysis and the mathematical fitting procedures. In Fig. S1 in the Electronic Supplementary Material (ESM), the isotopic abundances of Pd particles are shown. The errors between the calculated isotopic abundances, including also those for Ag and Fe experiments, and the reported values are all within 1%.

Pd and Ag (Figs. 3(a) and 3(b), respectively) particles were generated using the SDG$_C$ system at sintering temperatures of 500 and 250 °C respectively, which yield semi-sintered particles. The mass spectra of Fe particles that were generated using the same SDG system and sintered at 800 °C are shown in Fig. 3(c). The Fe mass spectra are dominated by the most abundant isotope, ^{56}Fe. However, along with the other Fe isotopes, FeO fragments can be detected. Note that, even if FeOs for each Fe isotope were present (i.e., ^{56}FeO, ^{54}FeO, ^{57}FeO, and ^{58}FeO) only ^{56}FeO is visible in Fig. 3(c) because of the corresponding signal strengths and the vertical-axis scale. The detection of oxidized ions means that Fe particles become partly oxidized during either synthesis or downstream processing (in this case, sintering at 800 °C), as will be described in greater detail below. Au particles were generated using the HTF (Fig. 3(d)). Cu particles were synthesized by SDG$_P$ but were not detected by the LV-AMS. A plausible reason for this is that Cu is easily oxidized and CuO does not absorb sufficient energy at the vaporization wavelength used in this study (1,064 nm).

Figure 2 (a) Example of HR data, where metal ions (^{107}Ag$^+$ in this case) are clearly separated from an organic ion fragment (impurity). (b) Mass defect vs. m/z plot showing the most abundant metal isotopes of the metals used in this work. Molecular fragments are fit to the HR mass spectra and examples of mass defects are apparent. The possible ion fragments shown here were not necessarily identified in any of the measurements. The ion fragments are divided into different families depending on their atomic composition.
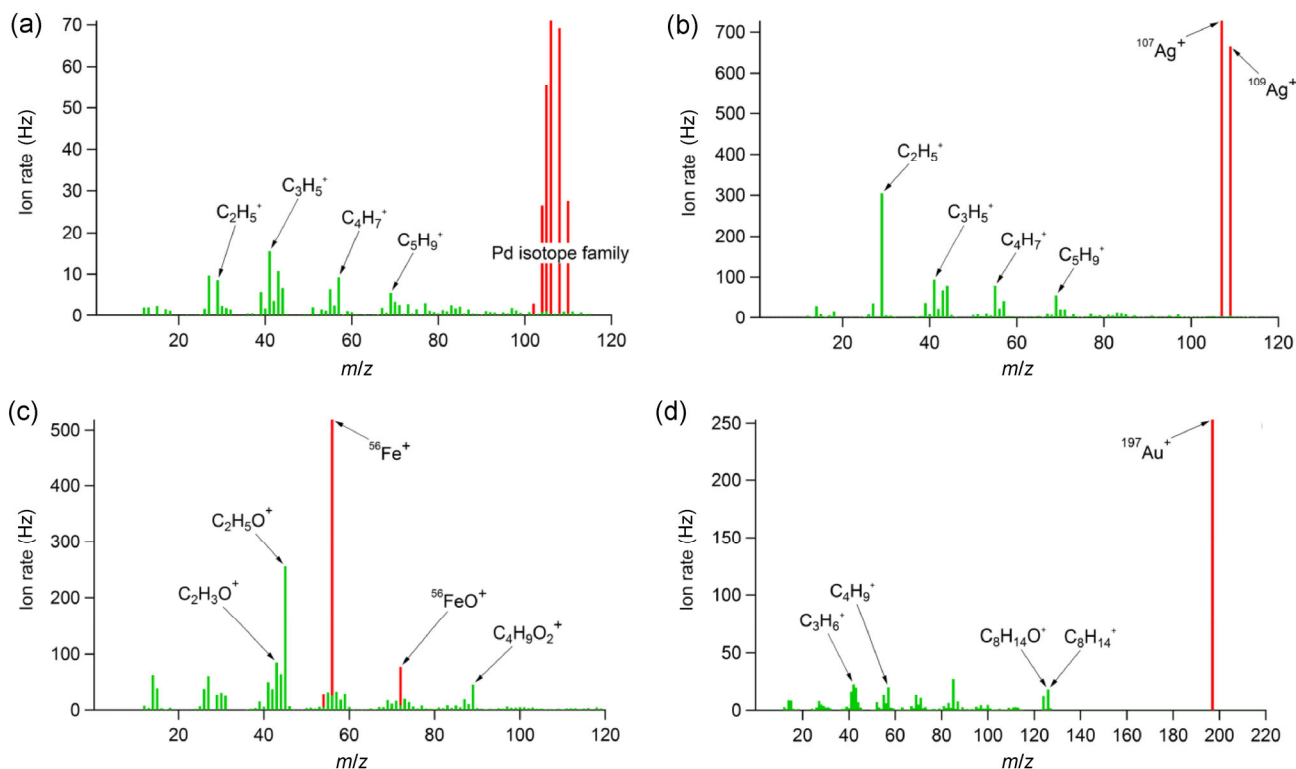
Figure 3 Mass spectra of four differently synthesized nanoparticles. Metal ions and fragments representing organic impurities are shown in red and green, respectively. (a) 100-nm semi-sintered Pd particles (SDG$_C$); (b) 100-nm semi-sintered Ag particles (SDG$_C$); (c) 110-nm sintered Fe particles (SDG$_C$); and (d) 40-nm sintered Au particles (HTF). The diameters are d_m.

3.3 Mass spectra of organic and inorganic impurities

The LV-AMS was used to explore the effects of the particle synthesis method, sintering temperature, and particle material on the impurity composition in the particle phase. As can be seen in Fig. 3, the organic impurities on the Fe particles differed from the organics found on both the Ag and Pd particles, even though these three particle types were synthesized using the same method and setup. The organic ion fragments detected on, or in, the Ag and Pd particles were typical for aliphatic hydrocarbons, while a higher fraction of O-containing fragments was observed in the case of the Fe particles. Explanations for this result were not investigated, but it is hypothesized that the presence of traces of O in the carrier gas, oxides on the Fe electrodes, the different sintering temperatures used, and/or differences in the particle surface properties led to adsorption of components with different polarities. The dominant organic fragment for Fe particles was found to be m/z = 45, identified as $C_2H_5O^+$.

The obtained HR mass spectrum of the organics on the aggregate Pd particles is shown in Fig. 4(a). It is apparent that, in the absence of sintering (20 °C), the organic mass spectrum is dominated by aliphatic fragments (C_xH_y) with an oxygen-to-carbon ratio (O/C) of 0.10. Note that the O/C calculation utilizes the improved ambient method for O/C ratio calculation presented by Canagaratna et al. [32]. The largest contributions were obtained for m/z = 41, 43, 55, and 57, which correspond to common alkane and alkene fragments. Using the LV-AMS, we observed that the O/C ratio decreased when a temperature greater than 100 °C was attained; this means that the relative contributions of oxygenated ions, such as CO_2^+ and CHO^+, decreased. This is shown in Fig. 4(b).

In a comparison of Au aggregate particles synthesized using the SDG$_P$ or HTF on the same day, significant differences in the mass spectra of the organic impurities were observed (Figs. 5(a) and 5(b)), with dominating contributions at m/z = 74 for the SDG$_P$ synthesis and m/z = 85 and 126 for the HTF case. The organics present on the Au particles formed in the SDG$_P$ appear to
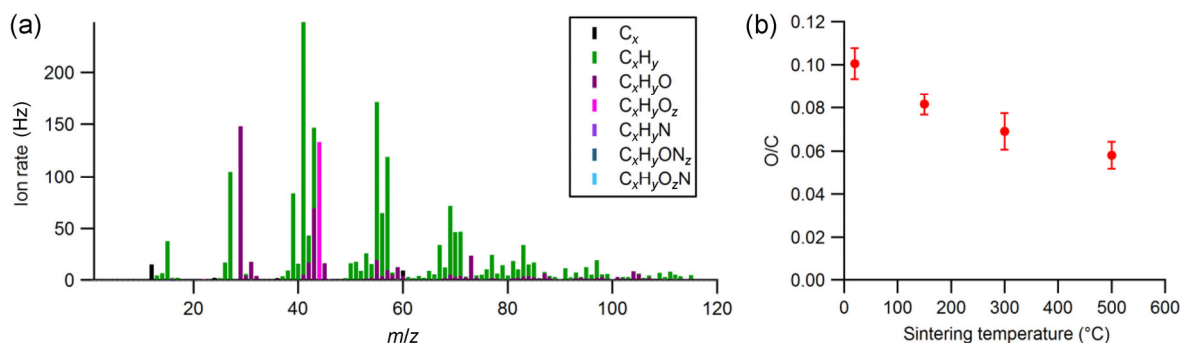
Figure 4 (a) HR organic mass spectrum for impurities on 100-nm Pd aggregate particles (sampled at 20 °C). The ion fragments are divided into different families depending on their atomic compositions. The m_{fOA} is dominated by $C_xH_y^+$ fragments. (b) O/C as a function of sintering temperature. The error bars show standard errors of means.
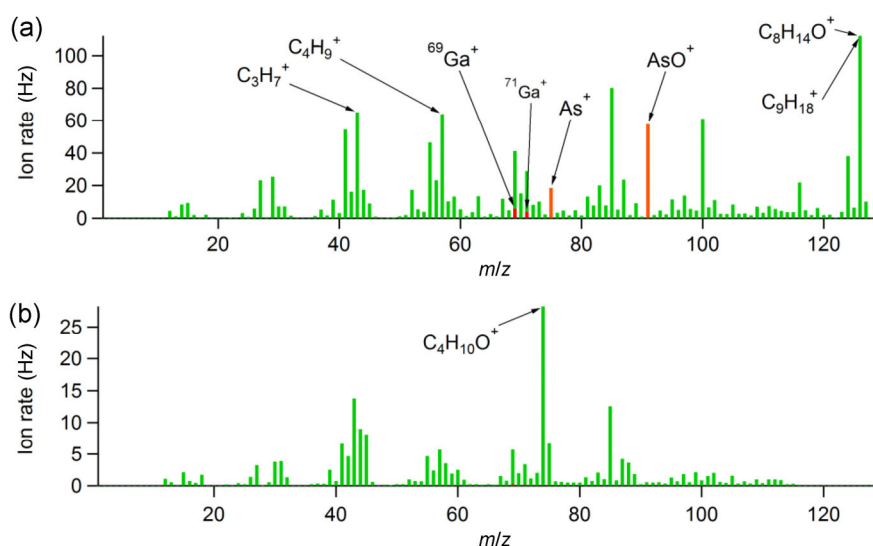

Figure 5 Unit mass resolution spectrum of impurities on 100-nm Au aggregate particles generated using (a) HTF and (b) SDG$_P$.

have had a higher oxygenated species content, while the organic species on the HTF-generated particles were primarily composed of aliphatic components. Messing et al. [33] previously concluded that the choice of synthesis method has little effect on the properties of nanowires for which synthesized Au particles are used as seed particles. However, in the abovementioned study, the Au particles were sintered at high temperature; thus, the possible effect of the organic coating on the end results was reduced, as the organic coating on the metal particles was minimized. If no sintering is performed or low sintering temperatures are used, our results indicate that the synthesized particles may have different surface properties in response to differences in the impurity composition.

Prior to the measurements with the LV-AMS, the HTF and sintering furnace were used to generate Au seed particles for GaAs nanowire growth in an aerotaxy system. After the aerotaxy system had been disengaged from both the HTF and the sintering furnace, HTF maintenance was deliberately neglected. This approach was taken in order to determine whether any traces of the materials supplied to the aerotaxy system could reach the HTF, even though the HTF was connected upstream of the aerotaxy system. The mass spectrum of the Au aggregates (Fig. 5(a)) synthesized using the HTF after the aerotaxy system had been disengaged exhibited both Ga and As components, with AsO$^+$ (m/z = 91.917) and As$_3$O$_4^+$ (m/z = 288.744) being the main fragments. Thus, the presence of Ga and As species inside the HTF demonstrates a need for maintenance of not only downstream equipment, but also upstream equipment in particle-generator setups.

Contamination of upstream equipment may lead to undesired synthesized particle behavior, as the chemical content and surface properties of the particles may be altered. The capacity to detect contaminations during the continuous production of nanoparticles in real-time is important in order to maintain, or enhance, production efficiency. *In-situ* characterization of the generated nanoparticles is a means of rapidly detecting undesired behavior within the synthesis process and equipment.

In summary, the LV-AMS has allowed us to demonstrate that the generator type, particle material, sintering temperature, and generator history may all affect the impurity composition in the particle phase. These measurements were conducted by directly sampling the particles from the aerosol-phase in the generator into the LV-AMS, thus, uncertainties related to the storage of collected material on the substrates were avoided. The aerodynamic lens inlet allowed us to concentrate the particle phase by approximately a factor of 10^7 relative to the gasphase, thus, the majority of the gasphase artifacts (less than ~10 ppm) could be safely neglected. In addition, the vapor pressures of organic components commonly found in the particle phase are sufficiently low that volatilization during transport in the vacuum chamber can be neglected.

3.4 Quantification of organic impurity coatings on metal nanoparticles

Figure 6 shows that the organic-impurity content on synthesized Pd particles decreases upon passage through the sintering furnace at increased temperatures. Here, m_{fOA} decreased from 4%–7% at sintering temperatures below 200 °C to less than 1% at a sintering temperature of 500 °C. The mass fractions of the impurities for the other investigated metals were similar as for the Pd particles. Measurements were also performed at a sintering temperature of 650 °C. At this temperature, the organic signal strength reached the 3σ of the LV-AMS; therefore, these results are not shown. Note that the 3σ for organic aerosol was 54 Hz, which corresponds to an organic aerosol mass concentration of 0.04 μg·m⁻³ if an RIE_{OA} of 1.4 and CE of 1 is assumed.

It is important to note that the impurity fraction for Pd particles does not drop to zero at temperatures
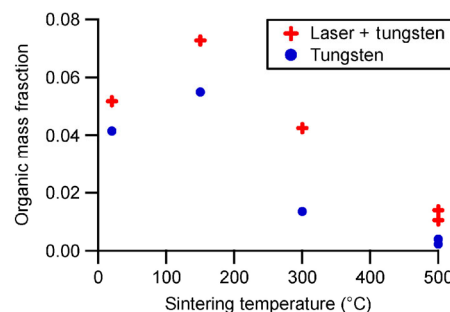

Figure 6 Ratio of m_{fOA} to total m_p for 100-nm (d_m) Pd particles as a function of sintering temperature. The results for the two vaporizer configurations are shown, assuming that CE = 1.

at which the majority of organic components would be expected to evaporate (500 °C). This observation was also made for the other examined materials. This suggests that the metal nanoparticles are strong absorbers of organics and/or that the organics are volatilized in the sintering furnace, and then a fraction of the organics re-condense upon exit.

A 0.5-nm organics monolayer with unit density around a spherical Pd primary particle with 5-nm diameter yields an m_{fOA} of approximately 6%. If it is assumed that the full surface areas of all primary particles in the aggregate are accessible for organic impurity uptake, the 6% value can be compared with our experimental observations of 4%–7% for non-sintered particles. Thus, based on our results, we hypothesize that a monolayer of organics may be present in many nanoparticle applications. As the particles are sintered, the accessible surface area decreases, which may partly explain the decreasing impurity mass fractions upon sintering.

The importance of the properties of the monolayer surrounding the aerosol particles investigated here, as regards to both technical applications (such as catalysis and nanowire/tube growth) and particle inhalation, requires detailed investigation. In this respect, note that the layer of biomolecules that binds to nano-particles upon deposition in bodily fluids has recently been suggested to constitute a key component of the subsequent nanoparticle interactions with the various target organs and intra-cellular trafficking. The properties of this layer may be more important than the properties of the bare metal nanoparticle themselves [34].

The *in-situ* sampling capability of the LV-AMS is of high importance when investigating organic surface coatings and impurities, as these components may be altered during the sampling, storage, or analysis required for conventional offline techniques. Conventional techniques to distinguish organic surface coatings from collected samples include thermogravimetry as a screening method [35]. In addition, the chemical analysis methods commonly used for the detailed examination of nanomaterial organic surface coatings include thermal desorption (TD) or accelerated solvent extraction (ASE), followed by gas chromatography (GC)-MS, matrix-assisted laser desorption/ionization (MALDI)-TOF-MS or electrospray ionization MS.

3.5   Detection of metal nanoparticle oxidation

The LV-AMS can be used to monitor changes in the degree of oxidation by measuring the signal strength of metal-oxide and pure metal ions. In this work, metal-oxide ion signals were successfully observed for synthesized Fe and Ni particles using the LV-AMS, whereas the Ag, Pd, and Au particles did not exhibit signals corresponding to ions containing both metals and O. The degree of oxidation of both the Fe and Ni particles increased with increasing sintering furnace temperature (Fig. 7).

An increase of the sintering temperature from 300 to 800 °C doubled the FeO^+ ion signal compared to that of the Fe metal ions. An even larger effect was observed for the Ni particles, where an increase from 400 to 700 °C increased the NiO signal fraction six fold compared to that of the Ni metal ions. The highest
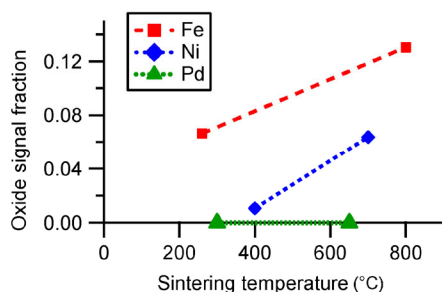
Figure 7   Oxide signal mass fractions of particles from three different metals as functions of sintering temperature. The oxide signal fraction is determined by the MO/(MO+M) ratio, where MO is the summed metal-oxide ion signal and M is the summed pure metal ion signal, assuming that the RIE and CE for metal and metal-oxide ions are identical.

sintering temperature used for the Pd particles was 650 °C. However, no PdO^+ fragments were found in the mass spectra at this temperature.

The degree of oxidation depends on factors such as the pre-existing metal oxide on the electrodes, O penetration into the synthesis setup, traces of O in the carrier gas or, possibly, oxidized organic components on the setup interior walls. Further examination of the origin of the detected O was not performed in this work. The likely explanation is that small amounts of air leaked into the synthesis systems at unidentified locations. Using the LV-AMS, we observed that the amount of O present in the synthesis setup and the employed temperature were sufficient to create Fe and Ni oxides, but not Pd and Ag oxides.

The degree of particle oxidation is important as regards the particle surface properties, and may be both a desirable and undesirable feature during particle synthesis. The segregation of active constituents to yield bimetallic nanoparticle surfaces, for example, has received considerable attention as a means of increasing the effectiveness of catalysts [36]. One method of achieving this is by introducing a reactive gas and applying heat to the synthesized particles. Blomberg et al. [36] studied the segregation of Pd in mixed PdAg particles by introducing traces of O_2 into the system. At elevated temperatures, surface oxides were formed and the Pd was found to segregate to the particle surface because of the favored formation of PdO over AgO. The LV-AMS can be used to track the degree of metal nanoparticle oxidation in such cases *in-situ* and as a function of sintering temperature. Hence, this technique allows optimal operating conditions for the synthesis of particles for a specific purpose to be determined. However, many metal oxides cannot be vaporized by a Nd:YAG laser, because of their small absorption cross-sections at 1,064 nm. For example, we did not obtain a detectable signal for the examined Cu nanoparticles, which was most likely due to the fact that the Cu particles were oxidized and CuO has a negligible absorption cross section at 1,064 nm. In this work, we have shown that FeO can be detected by the LV-AMS. Further investigation is required to determine whether or not FeO vaporization was achieved through laser absorption of the oxide itself or of pure Fe that then vaporized the oxide in

turn. Externally mixed metal oxides from black carbon (i.e., they are not contained within the same particle) may also occur in combustion emissions (oxides of Zn, Ce, V, etc.) and wind-blown dust emissions (FeO); thus, further studies of the suitability of the LV-AMS for applications involving metal oxides are required.

3.6 Detection of alloy nanoparticles

The SDG facilitates the synthesis of bimetallic particles with an alloyed structure using one electrode composed of each component. During the synthesis of PdAg particles, the Pd/Ag LV-AMS signal ratio was determined as a function of d_m in this study. The SDG_C was continuously operated at the same settings and differently sized particles were selected using the DMA. The results shown in Fig. 8 indicate that the Pd/Ag mass ratio is independent of particle size.

In repeated measurements, the LV-AMS yielded Pd/Ag ratios that were three times lower than those obtained using the reference method, PIXE (Table 1), under the assumption that both metals had the same mass-specific IE. Full quantification using the LV-AMS lies beyond the scope of this work. A hypothesis regarding the apparent underestimation of the Pd signal strength is that different relative ionization efficiencies apply to Pd and Ag. This hypothesis is supported by the fact that the ratio of the PIXE/LV-AMS measurements was constant, even though the alloy ratio differed by a factor of approximately two between the two different SDG instruments. Pd has a higher boiling point and lower vapor pressure than Ag. Therefore, it is also possible that the Pd was incompletely vaporized from these particles, which
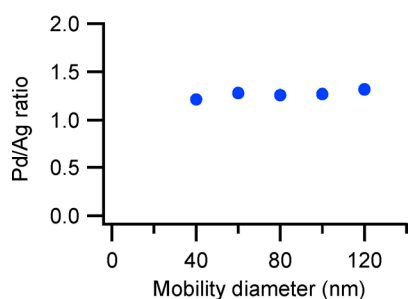
Table 1 Determined Pd/Ag ratio in PdAg particles

Generation method	SDG_P	SDG_P	SDG_C
PIXE	NA	2.5	1.2
LV-AMS	1.3	0.8	0.4
PIXE/LV-AMS	–[a]	3.1	3.0

[a]No PIXE-analysis filter samples were obtained during the first set of measurements. The LV-AMS was used to sample particles with different d_m.

may explain the lower detection sensitivity to Pd compared to Ag. In any case, these results indicate the potential of the LV-AMS technique as a method for the *in-situ* monitoring of the relative compositions of alloys and mixed-component nanoparticles.

3.7 Effect of sintering and organic coatings on equivalent particle sizes and densities

A key property of catalysts is the active surface available for the occurrence of heterogeneous reactions. A large surface-to-volume ratio is desirable, which renders nanoparticles optimal catalysts. The highest surface-to-volume ratio is achieved for complex aggregates generated through the coagulation of small primary particles. The primary particles can be fused together by bridging, and their structures determine the aggregate shape and density.

The synthesized metal nanoparticle sizes, physical structures, and shapes can be characterized *in-situ* in the aerosol phase via a tandem measurement of d_m using the DMA, followed by measurement of the d_{va} using the LV-AMS [37]. Sintering is a means of controlling the complexity of the overall particle shape and of eventually achieving spherical shapes. As the sintering temperature increases, the bridging between the primary particles within an aggregate becomes increasingly prominent and the particles become denser. This is illustrated in Fig. 9(a). In these experiments, the selected d_m of the processed particles was constant (100 nm). The d_{va}, on the other hand, increased with increased sintering temperature. The relationship between d_{va} and d_m (Eq. (3)) was used to determine the ρ_{eff} of the particles (Fig. 9(b)). Note that, to achieve near-spherical Pd particle shapes, a sintering temperature of 800 °C at minimum is required. In this set of experiments, however, the highest employed temperature was 500 °C; thus, the temperature was too
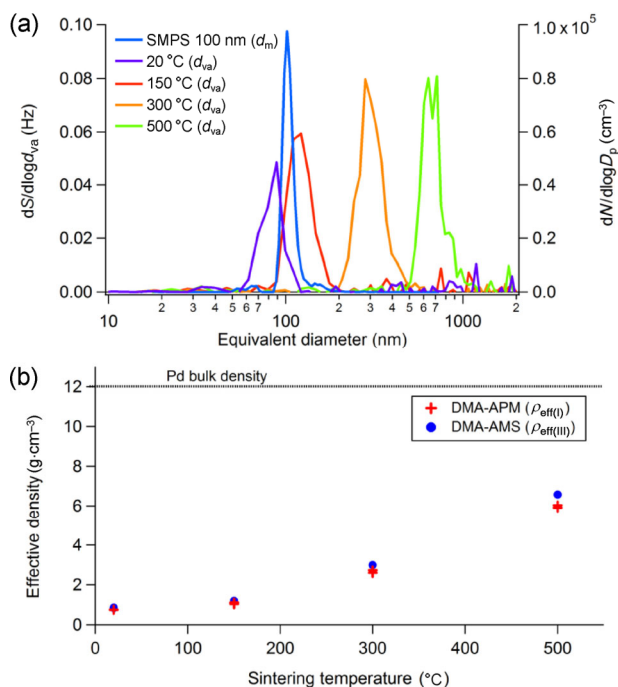

Figure 8 Pd/Ag ion signal ratio vs. d_m for internally mixed PdAg aggregates. The sintering oven was bypassed. The data indicated that the Pd/Ag ratio is conserved as the DMA-selected mobility particle size increases from 30 to 120 nm.

Figure 9 (a) LV-AMS size-resolved mass distributions for different sintering temperatures and Pd particles. The left y-axis shows the particle mass-weighted size distribution (in units of Hz) obtained with the LV-AMS. The blue line is the monodispersed particle size distribution measured with the SMPS and corresponds to the right y-axis. The d_m was fixed at 100 nm using a DMA positioned downstream of the sintering furnace, while the d_{va} of these mobility classified particles increased with sintering temperature. (b) ρ_{eff} calculated from DMA-LV-AMS and DMA-APM.

low to yield near-spherical shapes and a ρ_{eff} close to the inherent bulk density of Pd (12.02 g·cm^{-3}).

The measurement of ρ_{eff} using a combination of LV-AMS and DMA measurements provides a mechanism for monitoring the particle shapes and ensuring that they possess the desired morphologies. The capacity to measure two different equivalent diameters is also valuable if the synthesized metal particles are to be used for nanowire and nanotube growth. Depending on the sphericity of the seed particles, the achieved nanowires and nanotubes may exhibit different properties. In Fig. 9(b), two types of ρ_{eff} are shown, which were determined using two different methods. The most explicit method for the determination of ρ_{eff} is the DMA-APM measurement ($\rho_{eff(I)}$) as it involves direct measurement of m_p. The effective density values derived from the DMA-LV-AMS ($\rho_{eff(III)}$) measurements are slightly higher than the corresponding $\rho_{eff(I)}$ values.

Figure 10 shows that condensation of liquid organic

compounds for surface functionalization/coating affects $\rho_{eff(III)}$, and also the measured equivalent diameters of the nanoparticles. We used controlled condensation of a commonly used low-volatility organic liquid (DOS) on Ag nanoparticles with three different structures (aggregates, semi-sintered, and sintered) as a surface coating/functionalization model. All three types of Ag particles had the same initial m_p (4 fg). While an increased sintering temperature leads to an increased ρ_{eff}, organic-coating condensation often causes a decrease in this value. This is apparent in Fig. 10 for the sintered particle case, where the inherent material density of the condensing organic component is significantly lower than the material density of the metal-containing nanoparticle and, thus, the ρ_{eff} is lowered (Fig. 10(a)). However, for highly fractal aggregates, organic-surface-coating condensation initially leads to an increase in ρ_{eff}, because of a decrease in d_m (Fig. 10(b)). This is despite the fact that the initial ρ_{eff} is similar to the bulk density of the DOS, and is most likely due to surface-tension-enforced restructuring of the aggregate leading to a more compact shape. This results in a lower drag force and reduced equivalent d_m, as has previously been observed for atmospheric soot particles coated with H_2SO_4 [38]. The partly compacted aggregates are thereafter filled with the organic coating before full sphericity is achieved.

3.8 Limitations and recommendations for future research

For full quantification of metal nanoparticles using the LV-AMS, both the CE and the RIE$_s$ must be known. The CE factors that depend on losses in the inlet and focusing of the particle beam are more complex for metal than atmospheric particles. For example, E_L may be low for fully sintered particles (high density leads to high d_{va}) and E_S, which is related to the focusing of the particle beam, may deteriorate for aggregate particles. Future studies must focus on E_V, which is related to the fraction of the incoming particles that is vaporized when passing through the laser beam. Metals commonly have lower absorption cross sections at 1,064 nm compared to carbon black, for which the LV-AMS device was primarily designed. On the other hand, the vaporization temperature is
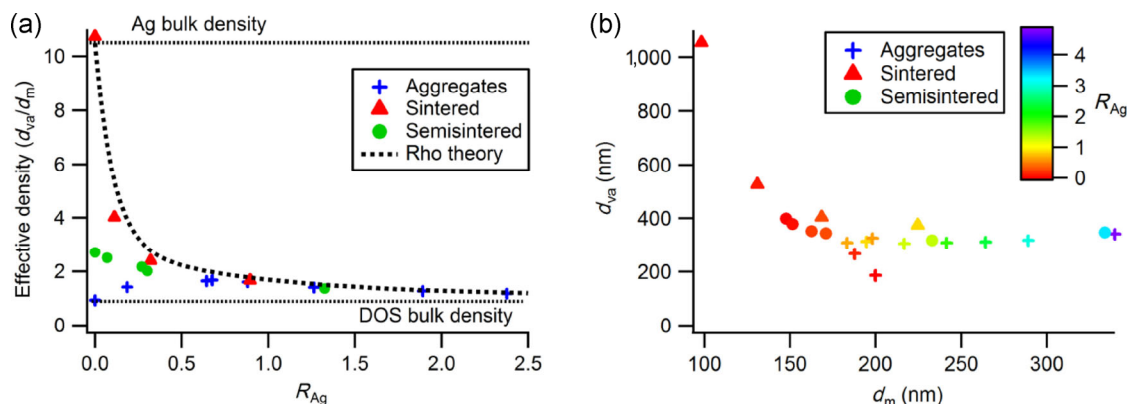
Figure 10 (a) Effective density ($\rho_{\mathrm{eff(III)}}$) as a function of the ratio of organic aerosol mass and Ag mass ($R_{\mathrm{Ag}} = m_{\mathrm{organics}}/m_{\mathrm{Ag}}$). The Ag mass was 4 fg for all three examined structures: aggregate, semi-sintered, and sintered particles. The dotted line (Rho theory) yields theoretically calculated densities assuming spherical particle shapes. (b) Equivalent particle diameters as a function of the ratio of organic total mass and Ag mass from experiments with various degrees of organic coating/surface functionalization.

lower for metals than carbon black and, as a result, the former may require less energy for vaporization. Carbone et al. (2015) have compared theoretically predicted and experimentally measured RIE at 70 eV (relative to C_3 carbon clusters from regal black aerosol) for metals that were internally mixed in the same particles as carbon black. The ratio between the measured and theoretical RIE was 0.28–1.08 for seven different metals (excluding metals where thermal surface ionization occurred). For the metal particles in this study, the highest obtained measured: theoretical RIE ratio, defined in the same way, was 0.5. This was obtained for Ag agglomerates coated with liquid DOS. However, as not only the RIE, but also the CE vary between the different metal particles and the calibrate particles (regal black), this comparison is complex and requires further study.

4 Conclusions

In this work, we have demonstrated that the LV-AMS can be used to characterize metal nanoparticles in the aerosol phase. Such *in-situ* characterization constitutes a means of minimizing sampling artifacts that can arise when particles are extracted from the aerosol phase and deposited on surfaces or substrates for subsequent offline analysis. We have shown that the LV-AMS can be used for the analysis of several key particle properties that determine the efficacy of metal-particle synthesis methods. These particle properties include particle chemical content (including impurity and metal-oxide analysis), particle mass-weighted size distributions, and particle compactness. The chemical content and composition of impurities present on the examined metal nanoparticles were found to differ depending on the employed synthesis method. Such differences may have an effect on the suitability of synthesized particles for their intended usage, if post-treatments such as sintering are not conducted. We found that contaminations originating from downstream equipment were present in the HTF. If *in-situ* characterization techniques are implemented in particle production processes, such undesired behaviors can be detected and handled in a manner that does not compromise the production efficiency. With the increasing demand for new aerosol nanoparticle synthesis methods, the development of new techniques that can be used for *in-situ* characterization of the produced nanoparticles is important. *In-situ* characterization methods, such as the LV-AMS technique, can be used for quality assurance and can aid understanding of nanoparticle formation processes. Nanowires (of metal or semi-conductors) constitute interesting nanostructures for future study.

Acknowledgements

within the framework of Metalund, the Centre for Medicine and Technology for Working Life and Society, supported by FORTE, the Swedish Council for Working Life and Social Research.

Electronic Supplementary Material: Supplementary material (isotopic abundances of Pd) is available in the online version of this article at http://dx.doi.org/ 10.1007/s12274-015-0877-9.

Open Access: This article is distributed under the terms of the Creative Commons Attribution License which permits any use, distribution, and reproduction in any medium, provided the original author(s) and source are credited.

References

[1] Kruis, F. E.; Fissan, H.; Peled, A. Synthesis of nanoparticles in the gas phase for electronic, optical and magnetic applications—A review. *J. Aerosol Sci.* **1998**, *29*, 511–535.

[2] Braakhuis, H. M.; Park, M. V. D. Z.; Gosens, I.; De Jong, W. H.; Cassee, F. R. Physicochemical characteristics of nanomaterials that affect pulmonary inflammation. *Part. Fibre Toxicol.* **2014**, *11*, 18.

[3] Buesser, B.; Pratsinis, S. E. Design of nanomaterial synthesis by aerosol processes. *Annu. Rev. Chem. Biomol. Eng.* **2012**, *3*, 103–127.

[4] Kulkarni, P. P.; Baron, P. A.; Willeke, K. *Aerosol Measurement: Principles, Techniques, and Applications*, 3rd ed; John Wiley & Sons: Hoboken, New Jersey, 2011.

[5] Messing, M. E.; Westerstrom, R.; Meuller, B. O.; Blomberg, S.; Gustafson, J.; Andersen, J. N.; Lundgren, E.; van Rijn, R.; Balmes, O.; Bluhm, H. et al. Generation of Pd model catalyst nanoparticles by spark discharge. *J. Phys. Chem. C* **2010**, *114*, 9257–9263.

[6] Blomberg, S.; Westerström, R.; Martin, N. M.; Lundgren, E.; Andersen, J. N.; Messing, M. E.; Gustafson, J. A high pressure X-ray photoelectron spectroscopy study of oxidation and reduction of Rh(100) and Rh nanoparticles. *Surf. Sci.* **2014**, *628*, 153–158.

[7] Murphy, D. M. The design of single particle laser mass spectrometers. *Mass. Spectrom. Rev.* **2007**, *26*, 150–165.

[8] Jayne, J. T.; Leard, D. C.; Zhang, X. F.; Davidovits, P.; Smith, K. A.; Kolb, C. E.; Worsnop, D. R. Development of an aerosol mass spectrometer for size and composition analysis of submicron particles. *Aerosol Sci. Tech.* **2000**, *33*, 49–70.

[9] Canagaratna, M. R.; Jayne, J. T.; Jimenez, J. L.; Allan, J. D.; Alfarra, M. R.; Zhang, Q.; Onasch, T. B.; Drewnick, F.; Coe, H.; Middlebrook, A. et al. Chemical and microphysical characterization of ambient aerosols with the aerodyne aerosol mass spectrometer. *Mass. Spectrom. Rev.* **2007**, *26*, 185–222.

[10] Cross, E. S.; Sappok, A.; Fortner, E. C.; Hunter, J. F.; Jayne, J. T.; Brooks, W. A.; Onasch, T. B.; Wong, V. W.; Trimborn, A.; Worsnop, D. R. et al. Real-time measurements of engine-out trace elements: Application of a novel soot particle aerosol mass spectrometer for emissions characterization. *J. Eng. Gas Turb. Power* **2012**, *134*, 072801.

[11] Eriksson, A. C.; Nordin, E. Z.; Nyström, R.; Pettersson, E.; Swietlicki, E.; Bergvall, C.; Westerholm, R.; Boman, C.; Pagels, J. H. Particulate PAH emissions from residential biomass combustion: Time-resolved analysis with aerosol mass spectrometry. *Environ. Sci. Technol.* **2014**, *48*, 7143–7150.

[12] Salcedo, D.; Onasch, T. B.; Aiken, A. C.; Williams, L. R.; de Foy, B.; Cubison, M. J.; Worsnop, D. R.; Molina, L. T.; Jimenez, J. L. Determination of particulate lead using aerosol mass spectrometry: MILAGRO/MCMA-2006 observations. *Atmos. Chem. Phys.* **2010**, *10*, 5371–5389.

[13] Zhang, Q.; Jimenez, J. L.; Canagaratna, M. R.; Allan, J. D.; Coe, H.; Ulbrich, I.; Alfarra, M. R.; Takami, A.; Middlebrook, A. M.; Sun, Y. L. et al. Ubiquity and dominance of oxygenated species in organic aerosols in anthropogenically-influenced Northern Hemisphere midlatitudes. *Geophys. Res. Lett.* **2007**, *34*, L13801.

[14] Salcedo, D.; Laskin, A.; Shutthanandan, V.; Jimenez, J. L. Feasibility of the detection of trace elements in particulate matter using online high-resolution aerosol mass spectrometry. *Aerosol Sci. Tech.* **2012**, *46*, 1187–1200.

[15] Onasch, T. B.; Trimborn, A.; Fortner, E. C.; Jayne, J. T.; Kok, G. L.; Williams, L. R.; Davidovits, P.; Worsnop, D. R. Soot particle aerosol mass spectrometer: Development, validation, and initial application. *Aerosol Sci. Tech.* **2012**, *46*, 804–817.

[16] Nilsson, P. T.; Isaxon, C.; Eriksson, A. C.; Messing, M. E.; Ludvigsson, L.; Rissler, J.; Hedmer, M.; Tinnerberg, H.; Gudmundsson, A.; Deppert, K. et al. Nano-objects emitted during maintenance of common particle generators: Direct chemical characterization with aerosol mass spectrometry and implications for risk assessments. *J. Nanopart. Res.* **2013**, *15*, 2052.

[17] Carbone, S.; Onasch, T.; Saarikoski, S.; Timonen, H.; Saarnio, K.; Sueper, D.; Rönkkö, T.; Pirjola, L.; Worsnop, D.; Hillamo, R. Characterization of trace metals with the SP-AMS: Detection and quantification. *Atmos. Meas. Tech.* **2015**, *8*, 5735–5768.

[18] Svensson, C. R.; Ludvigsson, L.; Meuller, B. O.; Eggersdorfer, M. L.; Deppert, K.; Bohgard, M.; Pagels, J. H.; Messing, M. E.; Rissler, J. Characteristics of airborne gold aggregates generated by spark discharge and high temperature evaporation furnace: Mass–mobility relationship and surface area. *J. Aerosol Sci.* **2015**, *87*, 38–52.

[19] Heurlin, M.; Magnusson, M. H.; Lindgren, D.; Ek, M.; Wallenberg, L. R.; Deppert, K.; Samuelson, L. Continuous gas-phase synthesis of nanowires with tunable properties. *Nature* **2012**, *492*, 90–94.

[20] Freund, R. S.; Wetzel, R. C.; Shul, R. J.; Hayes, T. R. Cross-section measurements for electron-impact ionization of atoms. *Phys. Rev. A* **1990**, *41*, 3575–3595.

[21] Dzepina, K.; Arey, J.; Marr, L. C.; Worsnop, D. R.; Salcedo, D.; Zhang, Q.; Onasch, T. B.; Molina, L. T.; Molina, M. J.; Jimenez, J. L. Detection of particle-phase polycyclic aromatic hydrocarbons in Mexico City using an aerosol mass spectrometer. *Int. J. Mass Spectrom.* **2007**, *263*, 152–170.

[22] Alfarra, M. R.; Paulsen, D.; Gysel, M.; Garforth, A. A.; Dommen, J.; Prévôt, A. S. H.; Worsnop, D. R.; Baltensperger, U.; Coe, H. A mass spectrometric study of secondary organic aerosols formed from the photooxidation of anthropogenic and biogenic precursors in a reaction chamber. *Atmos. Chem. Phys.* **2006**, *6*, 5279–5293.

[23] Drewnick, F.; Hings, S. S.; DeCarlo, P.; Jayne, J. T.; Gonin, M.; Fuhrer, K.; Weimer, S.; Jimenez, J. L.; Demerjian, K. L.; Borrmann, S. et al. A new time-of-flight aerosol mass spectrometer (TOF-AMS)—Instrument description and first field deployment. *Aerosol Sci. Tech.* **2005**, *39*, 637–658.

[24] Pöschl, U.; Martin, S. T.; Sinha, B.; Chen, Q.; Gunthe, S. S.; Huffman, J. A.; Borrmann, S.; Farmer, D. K.; Garland, R. M.; Helas, G. et al. Rainforest aerosols as biogenic nuclei of clouds and precipitation in the amazon. *Science* **2010**, *329*, 1513–1516.

[25] Matthew, B. M.; Middlebrook, A. M.; Onasch, T. B. Collection efficiencies in an aerodyne aerosol mass spectrometer as a function of particle phase for laboratory generated aerosols. *Aerosol Sci. Tech.* **2008**, *42*, 884–898.

[26] Willis, M. D.; Lee, A. K. Y.; Onasch, T. B.; Fortner, E. C.; Williams, L. R.; Lambe, A. T.; Worsnop, D. R.; Abbatt, J. P. D. Collection efficiency of the soot-particle aerosol mass spectrometer (SP-AMS) for internally mixed particulate black carbon. *Atmos. Meas. Tech.* **2014**, *7*, 4507–4516.

[27] Ehara, K.; Hagwood, C.; Coakley, K. J. Novel method to classify aerosol particles according to their mass-to-charge ratio—Aerosol particle mass analyser. *J. Aerosol Sci.* **1996**, *27*, 217–234.

[28] Park, K.; Cao, F.; Kittelson, D. B.; McMurry, P. H. Relationship between particle mass and mobility for diesel exhaust particles. *Environ. Sci. Technol.* **2003**, *37*, 577–583.

[29] Olfert, J. S.; Collings, N. New method for particle mass classification—The Couette centrifugal particle mass analyzer. *J. Aerosol Sci.* **2005**, *36*, 1338–1352.

[30] DeCarlo, P. F.; Slowik, J. G.; Worsnop, D. R.; Davidovits, P.; Jimenez, J. L. Particle morphology and density characterization by combined mobility and aerodynamic diameter measurements. Part 1: Theory. *Aerosol Sci. Tech.* **2004**, *38*, 1185–1205.

[31] Sleno, L. The use of mass defect in modern mass spectrometry. *J. Mass Spectrom.* **2012**, *47*, 226–236.

[32] Canagaratna, M. R.; Massoli, P.; Browne, E. C.; Franklin, J. P.; Wilson, K. R.; Onasch, T. B.; Kirchstetter, T. W.; Fortner, E. C.; Kolb, C. E.; Jayne, J. T. et al. Chemical compositions of black carbon particle cores and coatings via soot particle aerosol mass spectrometry with photoionization and electron ionization. *J. Phys. Chem. A* **2015**, *119*, 4589–4599.

[33] Messing, M. E.; Hillerich, K.; Bolinsson, J.; Storm, K.; Johansson, J.; Dick, K. A.; Deppert, K. A comparative study of the effect of gold seed particle preparation method on nanowire growth. *Nano Res.* **2010**, *3*, 506–519.

[34] Lundqvist, M.; Stigler, J.; Cedervall, T.; Berggård, T.; Flanagan, M. B.; Lynch, I.; Elia, G.; Dawson, K. The evolution of the protein corona around nanoparticles: A test study. *Acs Nano* **2011**, *5*, 7503–7509.

[35] Mansfield, E.; Tyner, K. M.; Poling, C. M.; Blacklock, J. L. Determination of nanoparticle surface coatings and nanoparticle purity using microscale thermogravimetric analysis. *Anal. Chem.* **2014**, *86*, 1478–1484.

[36] Blomberg, S.; Gustafson, J.; Martin, N. M.; Messing, M. E.; Deppert, K.; Liu, Z.; Chang, R.; Fernandes, V. R.; Borg, A.; Grönbeck, H. et al. Generation and oxidation of aerosol deposited PdAg nanoparticles. *Surf. Sci.* **2013**, *616*, 186–191.

[37] Park, K.; Dutcher, D.; Emery, M.; Pagels, J.; Sakurai, H.; Scheckman, J.; Qian, S.; Stolzenburg, M. R.; Wang, X.; Yang, J. et al. Tandem measurements of aerosol properties—A review of mobility techniques with extensions. *Aerosol Sci. Tech.* **2008**, *42(10)*, 801–816.

[38] Pagels, J.; Khalizov, A. F.; McMurry, P. H.; Zhang, R. Y. Processing of soot by controlled sulphuric acid and water condensation-mass and mobility relationship. *Aerosol Sci. Tech.* **2009**, *43*, 629–640.